Coalescence and fragmentation of colliding mercury drops

By A. MENCHACA-ROCHA[1], F. HUIDOBRO[1],
A. MARTINEZ-DAVALOS[1], K. MICHAELIAN[1],
A. PEREZ[1], V. RODRIGUEZ[1] AND N. CÂRJAN[2]

[1] Instituto de Física, Universidad Nacional Autónoma de México, AP 20-364, 01000 México DF, México
[2] CEN de Bordeaux-Gradignan, F-33170 Gradignan, France

Coalescence and fragmentation of equal and unequal liquid-drop pairs are studied using a new experimental technique in which mercury drops collide while sliding on a horizontal glass surface. The limits for coalescence measured as a function of the incident relative velocity and impact parameter are found to be similar to what has been reported for free-moving drops of other liquids, while new correlations are found to occur among the number, size, speed and angular distribution of fragmentation residues. The predictions of various models, including a dynamic theory originally developed for nuclear reactions, and specifically modified by us for macroscopic applications, are compared with the observations.

1. Introduction

Since the pioneering works of Plateau (1873) and Rayleigh (1882), collisions among pairs of liquid drops (henceforth simply referred to as 'drops') have been investigated extensively by meteorologists (e.g. Wang 1988) and atomization and spray experts (e.g. Yule & Dumouchel 1994). The evolution of this research up to 1970 was thoroughly reviewed by Park (1970), himself a major contributor, and up to 1978 by Pruppacher & Klett (1978). More recently, the works of Podvysotsky & Shraiber (1984), Ochs, Czys & Beard (1986), Ashgriz & Givi (1987), Brenn & Frohn (1989), Ashgriz & Poo (1990), Salita (1991), Jiang, Umemura & Law (1992), Menchaca-Rocha *et al.* (1993, see also Cuevas *et al.* 1993) and Qian & Law (1997) are good examples of the continued interest in this field. Reviews of the important works written in Russian may be found in the books of Vasenin *et al.* (1986) and of Sternin & Shraiber (1994).

To date, most quantitative experimental studies on 'direct' collisions (those in which liquid contact is established) have been aimed at determining the boundaries between two possible outcomes: 'coalescence' (one final drop) and 'fragmentation' (more than one final drop), as a function of the initial collision parameters, i.e. the relative velocity v_r, the 'impact parameter' b (measuring the centrality of the collision) and the type of liquid. However, concerning fragmentation, limitations inherent to the techniques used so far have prevented a detailed evaluation of final parameters, yielding mostly qualitative descriptions of the phenomena. Practical applications require a more quantitative understanding of the number, mass, speed and direction

of the fragments produced when two drops collide at a relative velocity sufficient for fragmentation.

Here we report on the results of 1000 binary drop collisions performed with an experimental technique based on the enhanced mobility found (Menchaca-Rocha 1992) for mercury drops laying on flat horizontal rough glass surfaces. This method allowed us to carry out detailed measurements of initial conditions (the two masses m_l, m_s and velocities v_l, v_s, of the large and small initial drops, respectively, and the impact parameter), shape evolution, and final conditions (the mass m_i, speed v_i and direction θ_i of the ith residue). As we shall see, besides a determination of the boundary between coalescence and fragmentation, this experimental method allows a more detailed study of the initial conditions necessary for fragmentation into a given number of residues (the 'multiplicity'), and to establish the correlations between various parameters, such as the speed of those residues and their emission angle, and between the energy loss, the impact parameter, and the relative velocity ($v_r = v_l - v_s$). Based on the similarities between our data and what has been reported for other liquids, we compare these results with predictions of a number of theories originally developed for free-moving drops, including a nuclear fragmentation model (Cârjan, Sierk & Nix 1986), which we have modified for macroscopic applications.

This work is organized as follows. Section 2 defines terms which are used in the text. To better appreciate the advantages and limitations of our method, a brief review of the techniques used so far in this field is presented (§ 3), before describing, in § 4, our experimental technique. Section 5 presents the experimental results obtained. Since these include observables which have been measured using more standard techniques, to illustrate the degree to which the present results can be generalized, in § 6 a comparison is made between our data and those available for other liquids. Concerning the theoretical situation, § 7 reviews the best known models in the field, comparing, when possible, their predictions with the data. Section 7 also presents the predictions of the dynamical model. The conclusions are summarized in § 8.

2. Definitions

Since our purpose is to further the understanding of the evolution and possible fragmentation of liquid masses formed in direct drop interactions, here the term 'collision' will exclude 'bouncing', a mechanism in which direct contact is prevented by the intermediate air film (Qian & Law 1997) Although interesting in its own right, for our purposes, this gas-drainage effect will be viewed as a complication, rather than as a source of information.

The most relevant parameters determining the outcome of this type of drop collisions in air have been found (Park 1970) to be: the initial drop masses m_l and m_s, the corresponding diameters D_l and D_s, the relative speed $|v_r|$ (or simply, v_r), the impact parameter b (figure 1), and the liquid's physical properties: density ρ, surface tension σ and kinematic viscosity v. The following dimensionless parameters can thus be defined: the diameter ratio $\Delta = D_l/D_s$ (henceforth referred to as 'size asymmetry', or just 'asymmetry'), the reduced impact parameter $B = b/\bar{D}$, where $\bar{D} = (D_l + D_s)/2$, and the Weber number $We = \rho \, d \, v_r^2/\sigma$, where d represents a particular choice of diameter (D_l, D_s or $\bar{D}$). When dealing with size-asymmetric systems ($D_l \neq D_s$), we shall use the $d = D_s$ convention, adopted by most authors in this field (Pruppacher & Klett 1978). Except for the recent works of Jiang *et al.* (1992), and Qian & Law (1997), who dealt with water and a variety of hydrocarbon compounds, little is known about the v-dependence of liquid drop collisions. Note that we chose to compare our

results (see §5) with those reported for liquids of similar kinematic viscosity so that, other factors being fixed, parameters depending explicitly on v, such as the Reynolds number $Re = \rho\, d\, v_r/v$, are not expected to vary significantly.

3. Review of experimental methods

The observation of collisions between pairs of drops moving in air involves two main techniques: the controlled production of fast moving drops, and the registration of a sequence of images from which the detailed analysis of the action can be made. To date, the most popular methods to generate drops for this type of experiment can be viewed as modern versions of the one proposed by Rayleigh (1882), who produced a fairly uniform stream of equally spaced equal-size drops by breaking up a water jet from a capillary which is mechanically excited using the vibrations of a tuning fork, later replaced by an electronic device. Since then, drop collisions have been observed by aiming two of those drop streams against each other. This technique produces drops with relative speeds in the $0.1 \leqslant v_r \leqslant 10$ m s^{-1} range. Faster ($v_r \leqslant 50$ m s^{-1}) drops of similar sizes have been obtained by Podvysotsky & Shraiber (1984) and by Menchaca-Rocha *et al.* (1986) using a technique based on capillary tubes soldered radially to hollow cylindrical shafts. The motor-driven horizontal rotation of those shafts causes a centrifugal flow of liquid through the capillaries leading to the production of droplets in the plane of rotation. A stream of well-separated liquid drops is then produced by selecting those moving in a given direction with the aid of a collimator. All of the above-mentioned techniques produce small ($D \leqslant 0.5$ mm) drops. Individual collisions involving larger ($1 \leqslant D \leqslant 5$ mm) drops were observed by McTaggart-Cowan & List (1975) through the use of vertical droplet accelerators combining gravitational and gas propulsion stages.

Collisions have been observed for drops approaching each other with a wide variety of relative orientations θ (see figure 1), from parallel ($\theta = 0°$), to antiparallel ($\theta = 180°$). Since the influence of terrestrial gravity causes all trajectories with horizontal components to have a parabolic shape, most experiments aim at reducing the local curvature to justify a straight-trajectory approximation. Under those conditions, the velocity vectors v_l and v_s define the collision plane. Thus, the initial collision parameters v_r and b are usually deduced from an analysis of images taken from a view perpendicular to that plane. Those images are obtained using fast photography, video- or cine-cameras. In the techniques used so far there is a coupling between the drop formation and the acceleration stage preventing a direct evaluation of the initial drop masses m_l and m_s. Thus the experimenters rely on values which are estimated by two methods: (*a*) dividing the amount of liquid collected from each droplet generator over a period of time by the number of droplets produced during the same period (e.g. Ashgriz & Poo 1990); (*b*) using the apparent drop size from pre-collision images (e.g. Brazier-Smith, Jennings & Latham 1972). The sizes of the collision fragments (or 'residues', i.e. all the drops formed after the collision), have also been obtained from photographic images (e.g. McTaggart-Cowan & List 1975).

The accuracy of these measurements places demands on a number of conditions, which can be difficult to fulfil. In the case of m_l and m_s, method (*a*) requires that the mass spectrum of the droplets has a narrow distribution, while in method (*b*) the distance from the droplet streams to the image-taking device should not change from drop to drop. Since the precise instant at which the initial drops come into contact is rarely registered, the determination of (*b*) is based on the assumption (Park 1970) that the drop trajectories are smooth and that the line of sight of the camera is strictly

perpendicular to the collision plane. A problem common to small-v_r measurements is that the droplets are often observed to approach each other slowly while falling in air at large speeds. In those conditions, not only does their motion occur in turbulent air, but the interaction between the droplets' wakes introduces distortions on the trajectories (Ochs *et al.* 1986).

Important progress has been made to understand and reduce these sources of uncertainty in the determination of initial conditions. Examples of this are the works of Park & Crosby (1965) and Brenn & Frohn (1989) concerning the influence of the liquid flow rate and the capillary oscillation frequency on the width of mass distributions, of Poo & Ashgiz (1991) on the influence of air drag on the drop stream, of Vassallo & Ashgriz (1991) on the formation of satellite drops in the breakup of the liquid jet, and of Adam, Lindbland & Hendricks (1968) who proposed a modification to the Rayleigh method in which the influence of the ambient air dragged along by the droplet streams is eliminated by electrostatically selecting out of the streams the individual droplet pairs to be observed. So far, however, little has been done to reduce the uncertainties associated with the determination of final parameters. For instance, the size of drops just after the collision, which is difficult to estimate from photographic plates since, in general, they are oscillating and rapidly moving away from the focal plane of the image-taking device. To our knowledge, collecting the individual residues for a direct evaluation of their size has not been attempted.

4. The mercury-drop collider

Some of the problems described in the previous section would be solved if a technique could be developed in which: (*a*) the mass of all droplets (initial and final) could be measured accurately, and (*b*) the position of all droplets could be followed in space as a function of time. One such technique is now described which is based on observing the interactions of mercury drops moving along a specially treated horizontal glass surface. We have built a liquid-drop collider (nicknamed 'Gotatron', where gota is Spanish for drop) to observe the interactions of mercury drops moving along a flat horizontal glass surface (figure 2), in which the drag induced by wetting is minimized by a roughening procedure which greatly reduced the mercury–glass contact. As described in detail elsewhere (Menchaca-Rocha 1992), this procedure results in a five-fold gain in the mobility of the mercury drops. Collision experiments involving mercury drops moving on solid surfaces have also been reported by Salita (1991). However, this interesting work was limited to 30 collisions, allowing only a rough determination of the coalescence–fragmentation transition, and giving no quantitative details about the fragmentation process.

In the Gotatron the initial drops of pre-determined masses m_l and m_s, are 'accelerated' to velocities $\boldsymbol{v}_l$ and $\boldsymbol{v}_s$ with the aid of 30° plastic ramps fixed on two extremes of the glass surface. A groove on each ramp guides the drops down the slopes and smoothly into straight horizontal trajectories. Each ramp can be rotated, orienting the drops' trajectories to be parallel and separated by an impact parameter b. The speed of the drops is varied by adjusting the height from which they are released. In this way, the outcome of the drop collisions can be studied as a function of b, v_r and $\varDelta$. The information, needed to determine the initial parameters $\boldsymbol{v}_r$ and b, as well as the speed v_i and direction of motion θ_i of each final drop i, is obtained by recording the action with a fast-shutter-speed (1/10 000 s) video system having a 30 frames s^{-1} recording frequency. As described in Menchaca-Rocha (1992), mercury drops moving on a glass surface do so as if subject to a (linear) velocity-dependent retarding force.
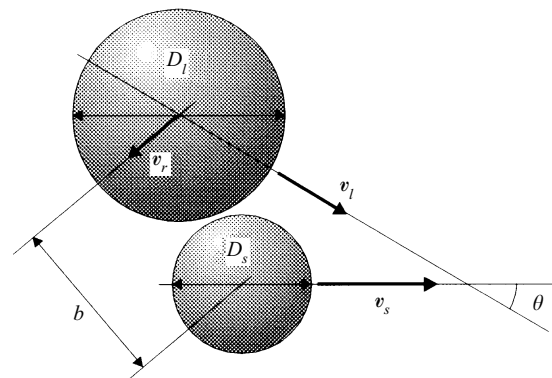
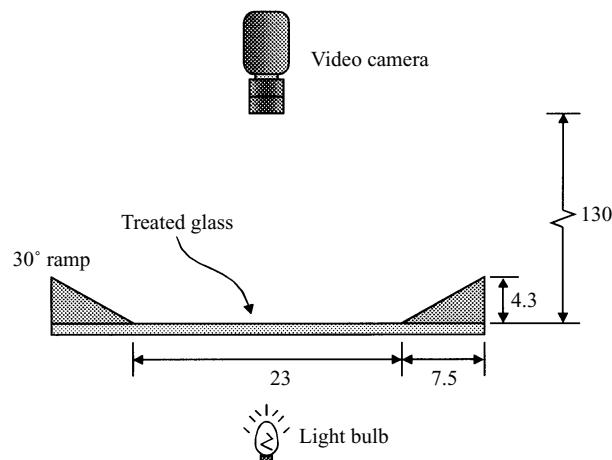FIGURE 1. Definition of the relevant geometric collision parameters.

FIGURE 2. Schematic diagram of the 'Gotatron'. All dimensions are in cm.

Thus, the equation of motion of every drop is determined through a minimum χ^2 fit to the position vs. time data to determine the initial speed and the deacceleration coefficient, which are relevant kinematic parameters. The uncertainty in the determination of speeds through this procedure is less that 5%. The final number of drops, the 'multiplicity' (N_f), is measured by counting all the drops formed after the collision; however, since secondary scattering (often leading to coalescence) among the primary fragments is not infrequent, a 'primary' multiplicity (N_p) can also be extracted by replaying the video images. The initial and final masses are measured with a 0.1 mg precision analytic scale. The values of all the parameters (initial and final) obtained in every collision (an 'event') were written in a computer data base, from which sorting routines were used to extract the statistics and parameter correlations presented in the next section. To our knowledge, this 'event-by-event' type of analysis, which is standard in other fields (e.g. nuclear and high-energy physics), had not been applied to drop collision experiments before.

For technical reasons (Menchaca-Rocha 1992), the Gotatron is limited to collisions of mercury drops having masses and velocities in the range $0.2 \leqslant m_{l,s} \leqslant 2.0$ g, and $5 \leqslant v_{l,s} \leqslant 50$ cm s^{-1}, respectively. The action of every drop-collision experiment lasts, typically, 1 s (i.e. 30 frames). Therefore the results presented in the next section

required the analysis of $\approx 30\,000$ frames. When the imaged area, of 19.2×14.4 cm^2, is digitized to 640×480 pixels, the initial drops are represented by ≈ 400 pixels. For simplicity, in the present study this volume of information is reduced by illuminating the action from underneath the glass surface (figure 2) and then extracting the drop contour information on each frame through standard image processing techniques. Figure 3 shows typical image sequences taken during coalescence and fragmentation collisions. More details about the drop 'acceleration' procedure used may be found elsewhere (Menchaca-Rocha 1992).

The main advantages of the Gotatron are: (*a*) it decouples the drop formation and the acceleration stages, permitting a precise measurement of the initial masses before acceleration; (*b*) because the motion is restricted to the horizontal plane, the final drops travel a finite distance along the glass surface and then stop, allowing us to collect them and weigh them individually; (*c*) restricting the motion to a plane eliminates the ambiguities introduced by out-of-plane components in three-dimensional motion, allowing more accurate determinations of the collision parameters from images taken from a fixed view; (*d*) the lack of vertical motion minimizes the velocity of the drops relative to air which, as mentioned before, is particularly important for small We measurements, and (*e*) compared with other liquids (water, glycerine, etc.), our larger D (≈ 5 mm) and higher density-to-surface tension ($\rho/\sigma = 3 \times 10^4$ s^2 m^{-3}) drops allow observations at lower v_r values for the same We, further reducing the influence of the ambient gas. As we shall see, measurements with larger drops also allow us to test the generality of the scaling variables used in this field.

The main disadvantages of this instrument are: (*a*) the mercury-glass interaction affects the drops' motion, (*b*) these, relatively large, drops oscillate around a non-spherical mean shape, (*c*) the drops 'roll' (Menchaca-Rocha 1992) (rather than slide) along the glass surface, and (*d*) compared to collisions among free-moving drops where the dynamics of the most central (small B) ones involve important out-of-plane components, in our case those components are strongly damped. We now discuss the importance of these effects.

First, we have shown (Cuevas *et al.* 1993) that, in the Gotatron, the drop–glass interaction is small when compared with the drop–drop interaction. To illustrate this, let us consider an 'inelastic' drop–drop collision, i.e. one in which the temporarily coalesced system undergoes a two-body fragmentation in which the final drop masses are very similar to the initial ones (as in figure 3*d*). This interaction favours our comparison since in it the amount of relative energy lost to internal degrees of freedom is small, compared with coalescence events, where all the relative energy is lost. Figure 4 shows a typical example of the time evolution of the total kinetic energy $E_T(t)$ (i.e. the sum of the individual kinetic energies) of drop pairs having $m_l = m_s = 1$ g. There are three distinct regions in the resulting $E_T(t)$ curve: (I) before, (II) during, and (III) after the collision. Extrapolating the strength of the drop–glass interaction from region (I), we find that the rate of kinetic energy loss during the collision is at least an order of magnitude greater than before, or after, the drop–drop contact.

Concerning oscillations, they have an arbitrary phase relative to the contact time, so that, for experiments with sufficient statistics, their main effect is to broaden the B-distribution. To minimize this problem, the collisions reported here were made to occur at a distance from the accelerating ramps sufficient to ensure at least a 60% reduction in the amplitude of those oscillations via viscous damping. The uncertainty in the determination of B was then quantified from an analysis of the pre-collision images by measuring the instantaneous eccentricity $\epsilon = (\alpha - \delta)/(\alpha + \delta)$ of the drops, where α, δ are the dimensions of the symmetry axes parallel and perpendicular to the drop velocity.
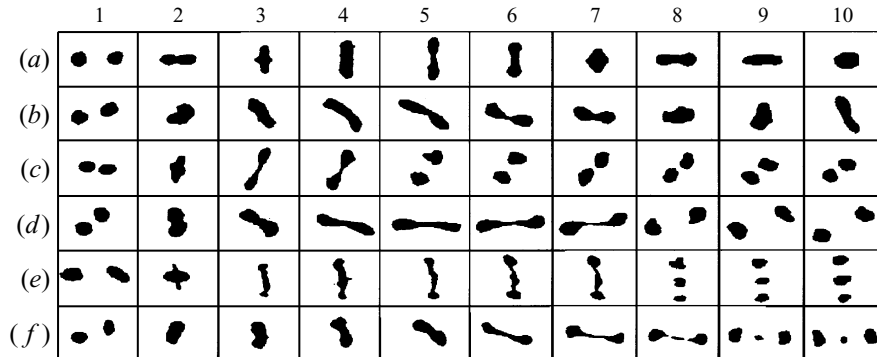
FIGURE 3. Time evolution of symmetric mercury-drop collisions: central coalescence in (*a*) and peripheral coalescence (*b*) small-*B* two- and three-body central fragmentation in (*c*) and (*e*), respectively: large-*B* two- and three-body peripheral fragmentation in (*d*) and (*f*), respectively. The drops move initially against each other in the horizontal direction, the time runs from left to right with $\Delta t = 1/30$ s from frame to frame. The [*We,B*] values corresponding to each time sequence are: [48.9,0.02] for (*a*), [15.2,0.58] for (*b*), [44.7,0.1] for (*c*), [25.0,0.82] for (*d*), [83.6,0.01] for (*e*), and [34.8,0.62] for (*f*).
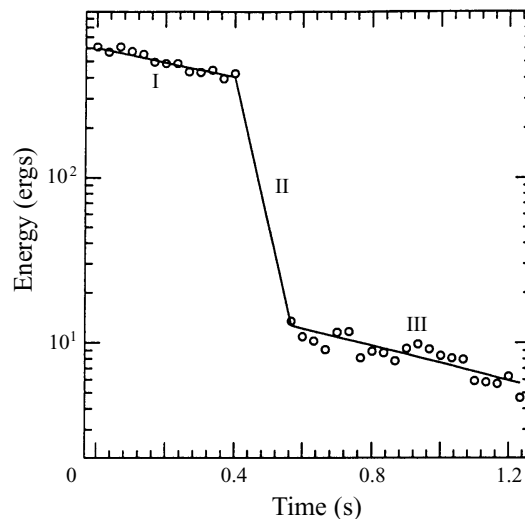

FIGURE 4. Evolution of the total energy measured (circles) before (I) and after (III) an inelastic drop–drop encounter (see figure 3*d*). The lines represent the best fit of an $E(t) = \frac{1}{2}\mu v_o^2 \exp(-(2\beta_i/\mu)t)$ parametrization which assumes the action of a velocity dependent friction force (see Menchaca-Rocha 1992), where v_o is the initial velocity, μ is the reduced mass, and β_i is the friction parameter. The rate of energy loss during the collision (II) was estimated by joining curves I and III, using the same parametrization. The friction coefficients used to draw the lines were $\beta_I = 0.5$ g s^{-1}, $\beta_{II} = 13.6$ g s^{-1}, and $\beta_{III} = 0.6$ g s^{-1}.

By assuming that, upon contact, the value of $\bar{D}$ to be used in the determination of $B = b/\bar{D}$ for deformed drops can be expressed as $2\bar{D} = D_l(1 - \epsilon_l) + D_s(1 - \epsilon_s)$, we used the standard deviation from the mean eccentricities ϵ_l and ϵ_s (of the large and small drops, respectively) to estimate the uncertainties in *B*. This effect depends on the mass and on the speed of the drops in such a way that, in our case, the maximum uncertainty in *B*, corresponding to the heavier and faster drops, does not exceed $\pm 10\%$, while the typical values are closer to $\pm 5\%$. The amplitude of these

oscillations upon contact turns out to be similar to that reported by Park (1970) for free-moving drops. To our knowledge, no other author has reported specific measurements of this sort. Note that for free-moving drops in which the masses are determined by the apparent size, oscillations add uncertainties which are not present in our experimental method.

The 'rolling' motion introduces a rotational energy, not always present in collisions between free-moving drops. Since the liquid masses rotate in opposite directions, upon contact the connecting neck is subjected to a 'twisting' motion which tends to lower its cohesive strength. As will be shown in §7, this disrupting effect is expected to be most important at the highest relative velocities. Still, the total angular momentum associated with this motion, which is parallel to the collision plane, tends to be small because of the opposite directions of rotation of the intervening drops. Note that there may be circumstances where the drop formation stage in free-moving drops actually imparts significant vorticity to the individual drops, so that the rotational energy present in the mercury–drop experiments may not be so different.

Finally, compared with collisions between free-falling drops, in the Gotatron the vertical motion is constrained by the glass surface. It has been observed (Ryley & Bennett-Cowell 1967) that small-B fragmentation occurs in two stages: (*a*) the formation of disks, and (*b*) the collapse, due to excess surface energy, of those disks into cylinders (in this case, collinear with the initial velocity vectors). The initial disks are due to an incompressibility-driven radial outward flow occurring along the contact plane. However, in our case the vertical component of this flow is rapidly projected back into the horizontal plane, leading to the formation of cylinders (not disks) in the initial stage, with their axis perpendicular (instead of parallel) to v_r. This effect precludes the direct comparison of the most central collisions between our results and those from drops moving in free space, particularly concerning the angular distribution of those residues. Still, if the viscous energy losses are comparable, the final outcome may be similar with respect to the mass, number and speed of the residues.

In spite of the complications just described, as shown in §6, the quantitative features we observe for mercury drops remain similar to those reported for collisions between free-moving drops.

5. Results

The data presented here result from the analysis of 1000 collisions, half of them for symmetric ($m_l = m_s = 1$ g) and the rest for asymmetric ($m_l = 1.5$ g, $m_s = 0.5$ g) pairs. Since these drops are non-spherical, we shall use the horizontally projected diameter to allow the comparison with collision data from spherical drops. This corresponds (Menchaca-Rocha 1992) to $D = 4.9, 6.5, 8.1$ mm for $m = 0.5, 1.0, 1.5$ g, respectively. Hence, for size-asymmetric systems we shall use $\Delta = 1.65$. The collisions were measured within the $20 \leqslant v_r \leqslant 90$ cm s^{-1} range. No systematic $v_r < 20$ cm measurements were done since that region is dominated by permanent coalescence. The maximum of $v_r = 90$ cm corresponds to the operational upper limit of the Gotatron (Menchaca-Rocha 1992). Some of the figures in this section contain theoretical predictions which will be presented in §7.

5.1. *Shape evolution*

Figure 3(*a–f*) illustrates the time evolution (from left to right) of typical coalescence (rows *a* and *b*), two-body (rows *c* and *d*) and three-body (rows *e* and *f*) fragmentation,

$\Delta = 1$, collisions. Rows (*a*), (*c*) and (*e*) correspond to central ($B \approx 0$) and (*b*), (*d*) and (*f*) to peripheral ($B \approx 1$) interactions. In our experimental situation, where aerodynamic effects (such as bouncing) are small, all central collisions below a certain critical *We* lead to coalescence. The top sequence (row *a*) is an example of a coalescence interaction observed just below that limit. Upon contact (between frames 1 and 2) a neck-like structure is formed. Eventually (3rd frame), incompressibility forces a flow perpendicular to the incident direction. This flow forms cylindrical shapes. Below the limiting-*We* condition, those cylinders develop an intermediate neck (5th frame) strong enough to support the flow-driven stretching. The subsequent evolution (frames 6 and beyond) shows a damping oscillatory motion with maximal elongations alternating between being parallel and perpendicular to the incident direction. As shown in row (*b*), off-centre coalescence interactions also form stretching cylinders, now rotating (frames 3 and 4), eventually developing intermediate necks (5th frame) which, below a certain *B*-dependent limiting *We*, are strong enough to support the inertial pull of the outer liquid masses. After reaching a maximal stretching stage (between frames 5 and 6), the shape evolution consists of a combination of (damping) vibrational and rotational motions. The initial stages of $B \approx 0$ two-body (row *c*) and three-body (row *e*) fragmentation are similar to the lower-*We* central coalescence interactions (see row *a*), with an initial perpendicular flow, forming stretched cylinders on which now one or two (or more) unstable necks evolve, eventually leading to the formation of two, three (or more) residues. Peripheral fragmentation (rows *d* and *f*) also evolve initially in a way which is qualitatively similar to the lower-*We* case (row *b*), except that stretching now leads to the formation of one or two (or more) unstable necks which break up into two, three (or more) residues.

The time sequences shown in figure 3 are qualitatively similar to what has been reported (e.g. Park 1970) for collisions of drops moving in free space in the same $We \leqslant 125$ regime, with the existence of critical limiting *We*-values for both peripheral and central interactions and the formation of stretched cylindrical configurations which, depending on *B* and *We*, can break into two, three or more fragments. As mentioned before, the most important difference occurs for $B \approx 0$ collisions (rows *c* and *e*). In free space, the outward flow (along the contact plane) leads to the formation of disk-like structures which eventually collapse forming the unstable cylinders (Ryley & Bennett-Cowell 1967). Thus, the residues are emitted in a direction parallel to the incident one. In our case, however, the initial flow is constrained by gravity to the horizontal plane, thus forming the unstable cylindrical configurations in the initial outward-flow stage (not in the subsequent collapse). Consequently, our $B \approx 0$ fragmentation residues are emitted in a direction perpendicular (instead of parallel) to the incident direction.

5.2. *Number of residues as a function of B and We*

The distributions of normalized impact parameter *B* and *We* values covered in the experiments are shown in figures 5(*a*–*d*) for $\Delta = 1$, and 5(*e*–*h*) for $\Delta = 1.65$, where they are classified by the primary multiplicity N_p of the collision. The boundary between coalescence and fragmentation is seen in figure 5(*a*) and 5(*e*) as a well-defined transition cutting diagonally across the *B* vs. *We* plane which (for a given *We*) defines an upper limit for coalescence. Alternatively (again, for a fixed *We* value) this diagonal transition appears as a lower limit for fragmentation (see figure 5*b*–*d*, *f*–*h*). From now on, this border between coalescence and fragmentation will be referred to as the 'C-F boundary'. The data points corresponding to $\geqslant 2$ multiplicities (see figure 5*a*–*d*, *e*–*h*) tend to group along diagonal regions with con-
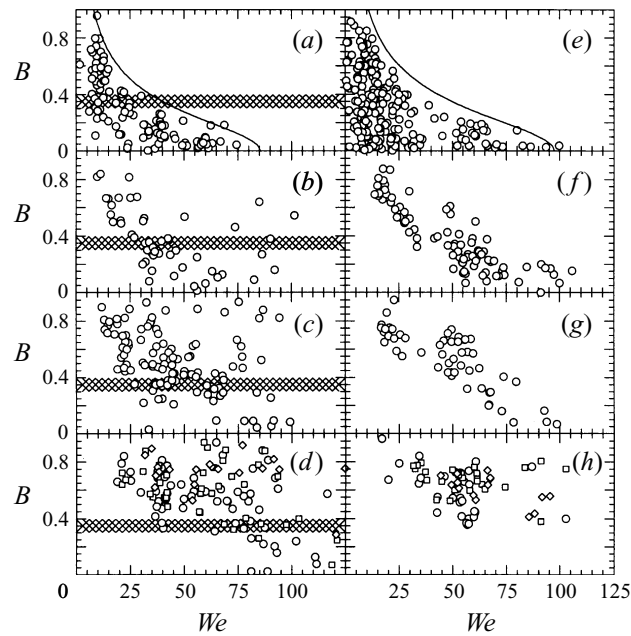
FIGURE 5. Mass-symmetric (left-hand column) and size-asymmetric (right-hand column) impact parameter vs. Weber number plots, for primary multiplicities $N_p = 1, 2, 3$, and $\geqslant 4$ in rows (a, e), (b, f), (c, g), and (d, h), respectively. In (d) and (h) the circles, squares, and diamonds represent $N_p = 4, 5$, and $\geqslant 6$, respectively. The hatched zones in $(a-d)$ show the ten regions used to locate the C-F boundary (see §6.1), while the solid lines represent the fitted curve using the parametrization described in §7.1.4.

siderable dispersion. Since the C-F boundary is better defined (see figure 5a,e), we do not associate this scatter with an experimental deficiency. There are aspects of the data represented in figure 5(b–d, f–h) which could explain this scatter: (a) the multiplicity does not contain information about the size of the residues, and (b) fragmentation is likely to be a non-linear phenomenon in which some variables could show a chaotic behaviour. Comparing figures 5(a–d) and 5(e–h) we also see that, for the same We value, the coalesced drops formed in size-asymmetric collisions seem to be more stable than their $\Delta = 1$ counterparts. The data in figure 5 also indicate a direct correlation between B and N_p. This is better illustrated in figure 6, where the mean impact parameter $\bar{B}$ is plotted as a function of the primary multiplicity N_p, for the three We windows indicated in the caption, in (a) for $\Delta = 1$ and in (b) for $\Delta = 1.65$. Note that, for a given $\bar{B}$ value, N_p increases with We.

The N_p-dependence of the (We- and B-integrated) frequency distribution of the residues' mass m_i (normalized to the total mass of the system $m_t = m_l + m_s$) is shown in figures 7(a–d) and 7(e–h) for $\Delta = 1$ and $\Delta = 1.65$, respectively. In both cases, fragmentation is found to produce two masses which are similar to the initial ones (the 'quasi-initial' residues), accompanied by tiny ('satellite') drops. This figure shows that the increment in multiplicity is linked to an increasing number of satellite drops, but seems to have little impact in reducing the gap between the different mass groups.
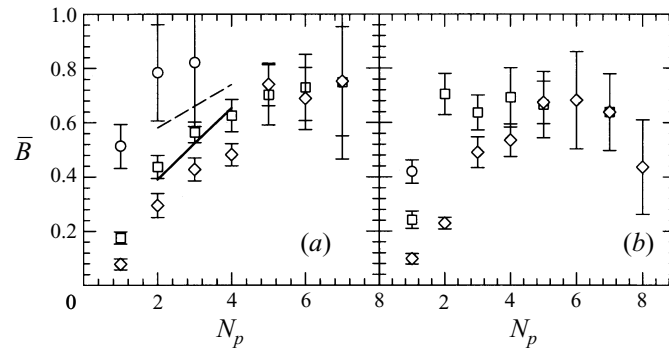
FIGURE 6. Mean impact parameter $\bar{B}$ plotted as a function of the multiplicity N_p and of We: (*a*) $\varDelta = 1$ and (*b*) for $\varDelta = 1.65$. The three We regions are: $We = 0$–15 (○), $We = 15$–60 (□), and $We = 60$–130 (◇). The error bars represent statistical uncertainties. The solid and dashed lines in (*a*) represent the $N_p = 2$–4 predictions of a fragmentation model described in §7.3.1, for ◇ and □, respectively.
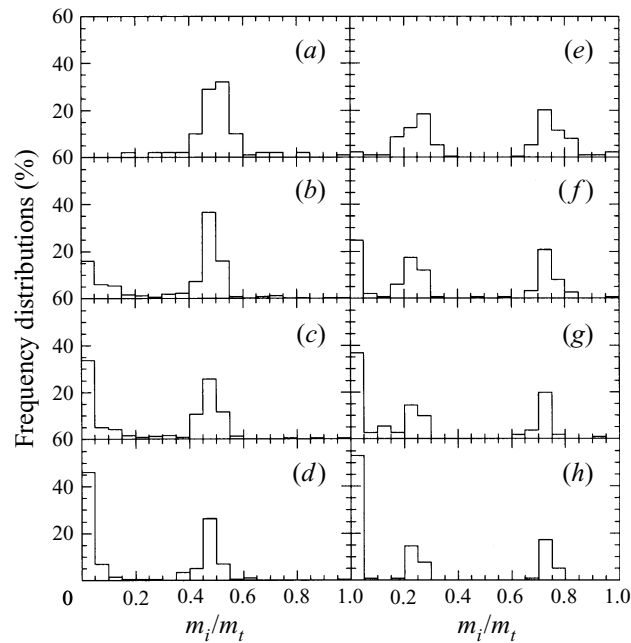

FIGURE 7. Fractional-mass frequency distributions for $\varDelta = 1$ (left-hand column) and $\varDelta = 1.65$ (right-hand column) systems, with $N_p = 2, 3, 4$ and $\geqslant 5$ in rows (*a, e*), (*b, f*), (*c, g*) and (*d, h*) respectively.

5.3. *Mass distributions*

Our experimental technique allows us to study the evolution of the residues' mass distribution with B and We, as illustrated in figure 8(*a–c*) for $\varDelta = 1$ and figure 8(*d–f*) for $\varDelta = 1.65$ collisions, using the same We windows as figure 6. As can be appreciated in (*a*) and (*d*) at the lowest We, coalescence ($m_i/m_t = 1$) dominates at all but the highest B, in (*a*), where fragmentation occurs leaving two masses similar to the initial ones (the quasi-initial residues), occasionally accompanied by satellite drops. The corresponding image sequences reveal that those satellite drops originate in the neck
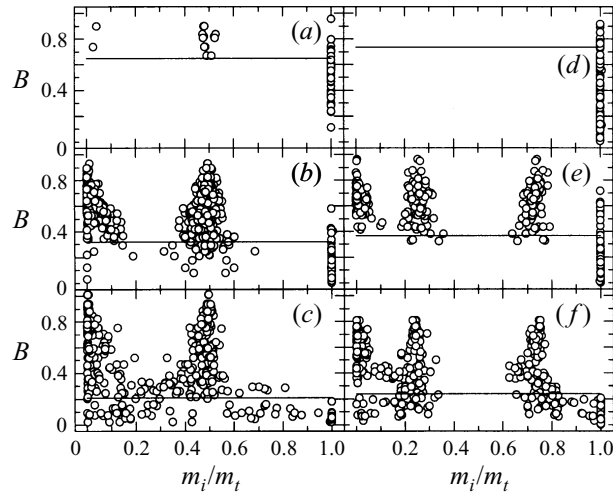
FIGURE 8. Residues' normalized masses as a function of B and We for $\Delta = 1$ (left-hand column) and $\Delta = 1.65$ (right-hand column) collisions, using the same We windows as in figure 6: (a, d) lowest values, (b, e) intermediate values, (c, f) highest values. The horizontal lines represent the lowest B_u two-body fragmentation limit of the corresponding We region, predicted by the Brazier-Smith *et al.* (1972) model (see § 7.1.2).

region. The lack of fragmentation in the high B-value region of (d) reflects again the higher stability of size-asymmetric systems. At intermediate We values (b, e), fragmentation extends to lower B-values, reducing the coalescence-dominated region to $B \leqslant 0.4$. We can now appreciate an impact-parameter dependence of the mass groups, such that, as B decreases down to the 0.4 region, in (b) and (c) the width of the $\Delta = 1$ quasi-initial residue group broadens symmetrically, while in (e) and (f) the separated quasi-initial groups approach each other. Below $B \approx 0.4$ in (c) the single (broad) quasi-initial group splits into two rapidly separating mass groups, while in (f) the gap between the quasi-initial groups also increases rapidly. Concerning the evolution of the satellite-drop mass group, as B decreases, this group splits in two components (more clearly seen in (b), one composed of very small drops, and the other having an increasing mass. The corresponding image sequences reveal that this new mass group is produced in three-lobed configurations (see figure 3e) in which a large drop is formed in the neck's centre region. In those situations, the smaller satellite drops are residues from the breaking up of the two necks.

5.4. *Other observables*

Another important feature of our experimental method is the possibility of finding correlations among the various parameters. Examples of this are shown in figure 9(a–c) where the speed v_i of each residue is plotted as a function of its direction θ_i, and in figure 9(d–f) where v_i is plotted as a function of B for size-symmetric $\Delta = 1$ collisions, using the same We windows as previous figures. Here the speed of the residues is normalized to the average speed of the incident drops (roughly $v_r/2$) and the deflection angle is measured from the initial direction (assuming axial symmetry). These figures show how the spatial distribution of residues evolves from a near-isotropic one, of slow moving residues (figure 9a), to a concentration of residues of all speeds along the forward ($\theta \approx 0°$) direction (figure 9c) at large We values, while figure 9(d–f) shows how the correlation between the speed of the residues and B increases with We.
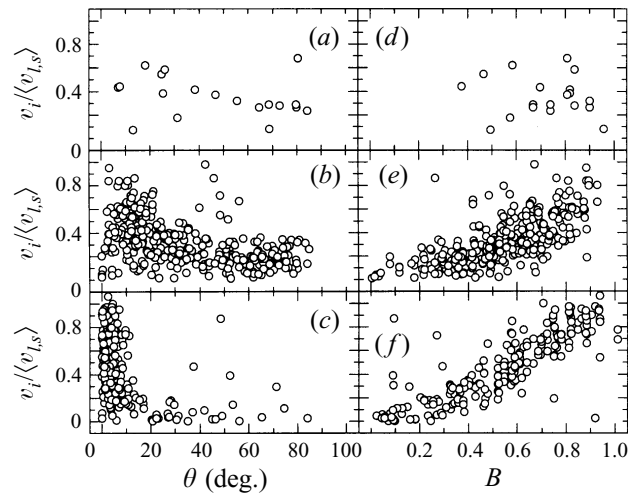
FIGURE 9. Residue speed v_i (normalized to the average speed of the incident residues) distribution for $\Delta = 1$ systems, shown as a function of deflection angle θ (left-hand column) and of B (right-hand column) collisions, using in (a,d), (b,e) and (c,f) the same three We regions, and in the same order, as in figure 8.

This type of data also allows a determination of indirect parameters such as the fraction of the total energy lost to dissipative processes

$$\Delta E = (E_i - E_f)/(E_i) \tag{1}$$

using $E_j = K_j + \sigma S_j$, where K_j represents the total initial ($j = i$) and final ($j = f$) kinetic energies and S_j the sum of the surface areas of all the drops at each stage (i or f), estimated from the drops' masses. This result is illustrated in figures 10(a–c) and 10(d–f), for $\Delta = 1$ and $\Delta = 1.65$, respectively, where we observe a correlation between ΔE and B, and how this correlation evolves with We. At the lower We values (figure 10a,d), where coalescence dominates (giving a constant ΔE), there is a significant gain in surface energy $\Delta S = S_i - S_f$, equivalent to $\approx 60\%$ of the total initial energy.

6. Comparison with other data

In this section we compare in more detail our observations with data obtained with standard experimental techniques, particularly concerning the limits for coalescence, as well as other aspects for which data exist. Limitations inherent to our technique prevent us from addressing other important issues such as the diffusion of mass, qualitatively investigated by Brazier-Smith *et al.* (1972) and by Ashgriz & Poo (1990) through the use colour-dyed water drops.

6.1. *The C-F boundary*

The existence of a well-defined boundary between coalescence and fragmentation in the B vs. We plane was first established by Adam *et al.* in 1968 (see their figures 4 and 6). As schematically shown in figure 11, at large B values this C-F boundary begins at a critical We_u value, below which all collisions (in which liquid contact is established) lead to permanent coalescence. Beyond We_u, the C-F boundary typically adopts a $B_u \propto We^{-1/2}$ dependence, which we shall call the 'upper' C-F branch. Some
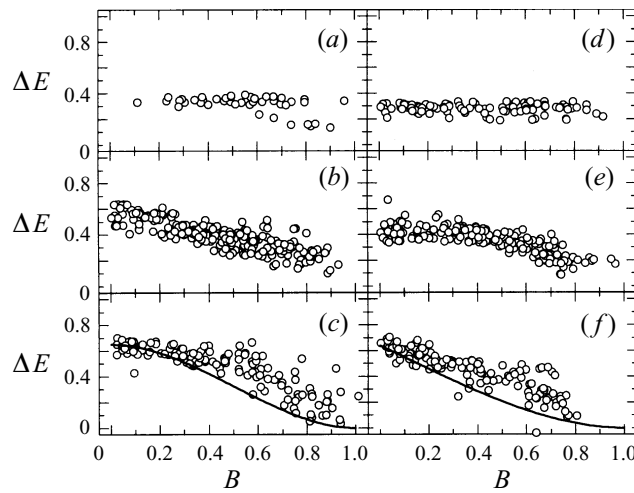
FIGURE 10. Impact parameter and *We* dependence of the fractional energy loss ΔE for $\Delta = 1$ (left-hand column) and $\Delta = 1.65$ (right-hand column) collisions, using the same *We* regions, and in the same order, as in figure 8. The solid curve represents the *B*-dependence expected when the energy loss is assumed to be proportional to the overlapping volumes (see §7.2)
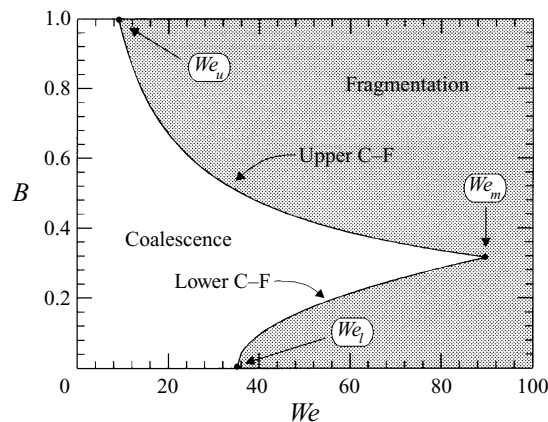

FIGURE 11. Schematic representation of the important boundaries and critical points defining the limits of coalescence in the *B* vs. *We* plane.

experiments indicate that a second critical value We_l appears at $B = 0$, beyond which fragmentation also occurs. As *We* is increased, this fragmentation mode extends towards non-zero impact parameters following a (not well established) increasing function of *We*, which we will call the 'lower' C-F branch, B_l. When observed, this branch is reported to merge into the upper branch at $B \approx 0.3$. Such crossing defines another important critical value, We_m, beyond which coalescence ceases to be observed.

Since, as to be explained in §7, the mechanisms determining the upper and lower C-F branches are generally thought to be different, the present discussion will be made separately for the upper and lower C-F branches. It is important to note that the data to be compared are not always presented in the same form. Some of them (including ours) consist of sets of values for the binary 'outcome' (coalescence or
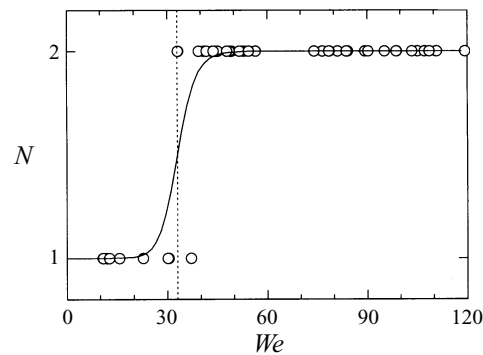
FIGURE 12. The outcome variable $N(We, B)$, extracted from the $\bar{B} = 0.35$ bin (hatched zones in figure 5) as a function of We. $N = 1, 2$ circles represent coalescence and fragmentation events, respectively. The solid curve results from a fit (see §6.1) used to determine the critical We_u (dashed line).

fragmentation) variable plotted in the B vs. We plane, from which the position of C-F boundary can be deduced, while other authors present direct C-F boundary data. Thus, a comparison of the available data requires a procedure to extract the C-F information from 'outcome' data. For that purpose we have used a method in which the outcome of the collisions is, first, associated with a binary variable $N(We, B)$, such that $N = 1$ indicates coalescence (only one final drop) and $N = 2$ indicates fragmentation (two or more drops). Then, pairs of coordinates (We_i, B_i) along the $N = 1 \leftrightarrow 2$ transition can be extracted by fixing one of the variables (We or B) and scanning on the other (e.g. hatched zones on figure 5a–d). Note that the (sometimes observed) two-branch structure of the C-F boundary makes the scanning on We (i.e. 'binning' on B) a simpler choice, since in that perspective the $N = 1 \leftrightarrow 2$ transition is single-valued. The mean critical We_i corresponding to each B_i bin can then be extracted by fitting a $N_i(We) = 2 - \{1 + \exp[(We - We_i)/a]\}^{-1}$ function (see figure 12, corresponding to the hatched regions in figure 5a–d), leaving We_i and a as free parameters, the latter being a measure of the uncertainty of the former. In our case, to guarantee sufficient statistics (≈ 50 'outcome' values) per bin, the B-axis was subdivided in ten equal-size bins. The resulting C-F boundary data from our mercury-drop experiments are shown in figures 13(a) and 13(b), for the $\Delta = 1$ and $\Delta = 1.65$ data, respectively. The error-bars shown in We correspond to the fitted a values, while those in B reflect the uncertainty due to oscillations (see §4).

The other 'outcome' data sets to be considered in this comparison, namely those from Park (1970) and Ashgriz & Poo (1990), correspond to measurements taken at fixed We values while varying B continuously (typically 20 'outcome' values), making the binning on We a natural choice. Since, in this case, the $N = 1 \leftrightarrow 2$ transition is double-valued, two $N_i(B_i) = 2 - \{1 + \exp[(B - B_i)/a]\}^{-1}$ fits per We bin were necessary to locate the position of the upper and lower C-F branches.

Concerning the procedures used by other authors to extract direct C-F data, Adam *et al.* (1968) analysed photographic image sequences from water-drop collisions to determine the impact parameter and relative velocity, and then applied a non-described averaging procedure among 'fifteen to twenty' collisions to determine points along the C-F boundary (no error-bars are given). Brazier-Smith *et al.* (1972) made on-line measurements of the C-F boundary by, at fixed We values, varying the lateral displacement (taken as a measure of b) of the two parallel drop streams, and looking
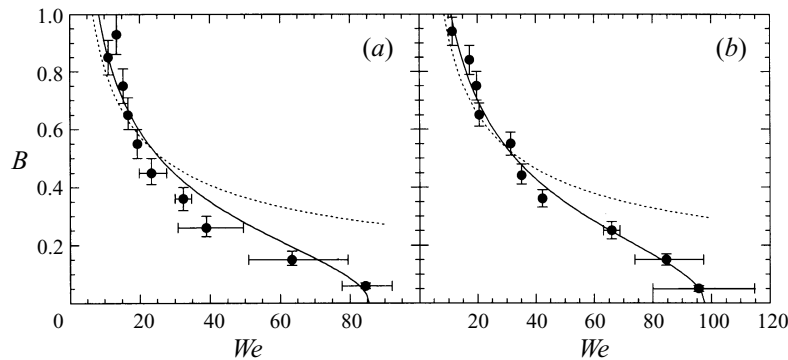
FIGURE 13. The C-F boundary extracted from the $\Delta = 1$ (a) and $\Delta = 1.65$ (b) mercury-drop data of figures 5(a–d) and 5(e–h), respectively, using the procedure described in §6.1. The curves represent the general behaviour observed for collisions in space (dashed) and how we expect it to be affected by 'rolling' (solid) (see §7.1.4).

for the critical value at which coalescence gives way to fragmentation. Although no error bars are quoted on each point, these measurements (see figure 7 of Brazier-Smith *et al.* 1972) show large fluctuations ($\geqslant 60\%$ at low *We*). Finally, Brenn & Frohn (1989), and Jiang *et al.* (1992), who also report direct C-F measurements, give no details on how they were obtained or the uncertainties involved.

6.1.1. *The upper C-F branch*

The *B* vs. *We* data sets from other authors are shown in figures 14(a–f) and 15(a–d), for size-symmetric and size-asymmetric collisions, respectively. As can be observed, there is a qualitative similarity between them, showing a typical

$$B_u = (We_u/We)^{1/2} \tag{2}$$

dependence (solid curves), where the We_u is the value of *We* at $B_u = 1$. The common shape of the upper C-F branch allows us to reduce the comparison to the relative values of one parameter, We_u, obtained from a fit to the data using equation (2). In §7 we see how the deviation from this $B_u \propto We^{-1/2}$ behaviour found in the low-*B* (high-*We*) region of the mercury data can be understood as due to 'rolling' (solid curves in figure 13). Note that at $B = 1$ both predictions (dashed and solid curves) are very similar. In figure 16(a) we plot the We_u values obtained for all the $\Delta = 1$ data as a function of *D*, while in figure 16(b) we show how that parameter varies with Δ. In (a) the data corresponds to cases for which the drop diameters are known, namely the water data of Adam *et al.* (1968), the propanol data of Brenn & Frohn (1989), the data of Park (1970), the water data of Jiang *et al.* (1992), the water data of Brazier-Smith *et al.* (1972), and the present mercury data. The horizontal lines represent the mean experimental value and its uncertainties. In (b) the open symbols correspond to the mean experimental values, and the full symbols to our mercury data. The $\Delta = 1$ values are taken from figure 16(a), while the $\Delta > 1$ points correspond to $\Delta = 1.33$ data by Ashgriz & Poo (1990), our $\Delta = 1.65$ mercury measurement, the $\Delta = 1.75$ data from Brazier-Smith *et al.* (1972), the $\Delta = 2$ are an average from the corresponding data of Park (1970) and of Ashgriz & Poo (1990), and the $\Delta = 3$ are data from Park (1970). The lines represent the predictions of models by Brazier-Smith *et al.* (1972), by Schmidt & Lutz (1992), by Park (1970), and by Arkhipov, Vasenin & Trofimov (1983).
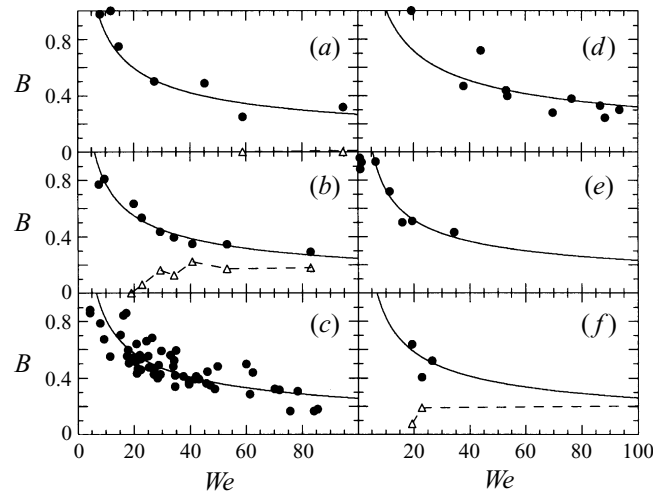
FIGURE 14. Comparison of available B vs. We, $\Delta = 1$, measurements: (*a*) the data of Adam *et al.* (1968) for $D = 120$ and 600 μm water drops; (*b*) the $D = 200$–1000 μm the data deduced (see §6.1) from the water data of Ashgriz & Poo (1990); (*c*) the $D = 300$–1500 μm data of Brazier-Smith *et al.* (1972); (*d*) the $D = 72, 100, 160$ and 200 μm propanol data of Brenn & Frohn (1989); (*e*) the $D = 300$ μm water data of Jiang *et al.* (1992); (*f*) the $D = 200$ and 700 μm data deduced from the water measurements of Park (1970). The ● correspond to upper C-F data, while the △ are lower C-F data. The solid curves represent a $B_u = (We_u/We)^{1/2}$ fit to the ●, leaving We_u as a free parameter. The dashed lines are drawn through the △ to guide the eye.
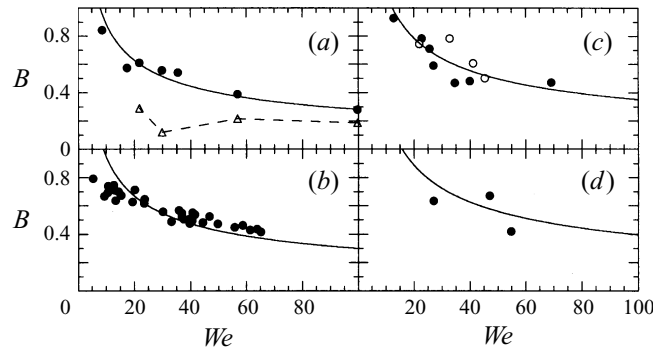

FIGURE 15. Comparison of available B vs. We, $\Delta > 1$, (all water) measurements: (*a*) $\Delta = 1.33$ data deduced (see §6.1) from the measurements of Ashgriz & Poo (1990); (*b*) the $\Delta = 1.75$ data of Brazier-Smith *et al.* (1972); (*c*) the $\Delta = 2$ data deduced from the data of Ashgriz & Poo (1990, solid symbols) and the data of Park (1970, open symbols); (*d*) the $\Delta = 3$ data of Park (1970). The ● and ○ correspond to upper C-F data, while the △ are lower C-F data. The solid curves show the fit to the (●) using equation (2) leaving We_u as a free parameter. The dashed lines are drawn through the △ to guide the eye.

Figure 16(*a*, *b*), shows that the We_u values measured from mercury-drop experiments are consistent with those found for other liquids using standard experimental techniques. Although there is a significant dispersion, the data also indicate the adequacy of We as a scaling variable for $\Delta = 1$ collisions. Note that our mercury data allowed us to extend this verification one order of magnitude in D.
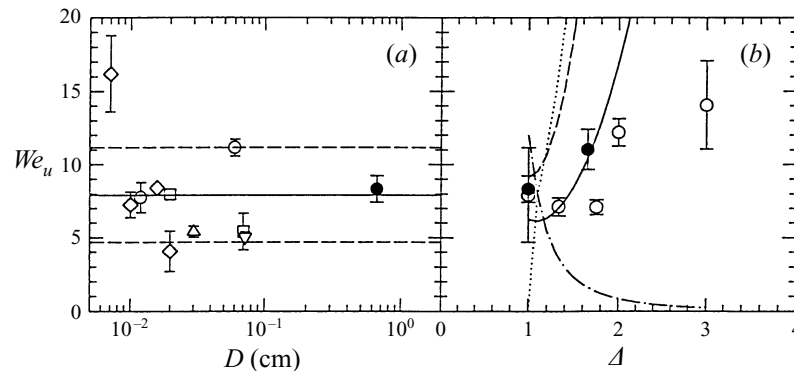
FIGURE 16. Diameter (*a*) and asymmetry (*b*) dependence of We_u obtained from the data in figures 13, 14 and 15. In (*a*) are shown the data of Adam *et al.* (1968, ○), Brenn & Frohn (1989, ◇), Park (1970, □), Jiang *et al.* (1992, △), Brazier-Smith *et al.* (1972, ∇), and the present mercury data (●). The horizontal lines represent the mean experimental value (solid) and its uncertainties (dashed). In (*b*) the ○ correspond to mean experimental values (including data from other authors), and the ● to our mercury data. The lines represent the predictions of models (see §7).

6.1.2. *The lower C-F branch and the We_l and We_m limits*

As mentioned before, in central collisions a second critical value We_l defines the limit for $B = 0$ coalescence. From that point in the B vs. We plane fragmentation extends to the small-(non-zero) B region following an (as yet undefined) direct function of We: the lower C-F branch. Thus, the point where the upper and lower C-F branches cross defines We_m, the highest We for coalescence (independent of B).

Although our experimental method introduces a distorting effect in the low-B region which prevents us from drawing conclusions on this aspect from the present mercury-drop data, we would like to comment briefly on the situation concerning the available data from collisions in space.

First, the values of the zero-impact-parameter limit We_l vary widely. For example, in the case of $\Delta = 1$ water systems, Ashgriz & Poo (1990), as well as Park (1970), report $We_l \leqslant 20$, while Adam *et al.* (1968) found values in the $We_l = 60$–100 range. The origin of such discrepancies may be linked to the vapour content of the ambient gas, as recently demonstrated by Qian & Law (1997).

Secondly, the situation concerning We_m is also intriguing. The only measurements showing this limit, those of Adam *et al.* (1968), yield $We_m \approx 100$ for small ($D = 120$ μm) and $We_m \approx 450$ for larger ($D = 600$ μm) drops. This result would indicate that, contrary to intuition, the temporary system formed by two small drops is less stable than that formed by bigger ones. It should be added that no other measurements, including those of Brenn & Frohn, reaching $We \approx 480$, for $D = 160$ μm propanol drops, have established a high-We limit for coalescence. Clearly this situation deserves further investigation.

6.2. *Other observables*

The other drop-collision parameters which have received some attention are the residue mass and multiplicity distributions. Measurements for $\Delta > 1$ by List, MacNeil & McTaggart-Cowan (1970), McTaggart-Cowan & List (1975), and Bradley & Stow (1979) for water drops and by Arkhipov *et al.* (1983) for water glycerine solutions, showed that, as in our case (e.g. compare figure 7*e*–*h* with figure 6 of List *et al.* (1970) and figure 1 of Bradley & Stow 1979), the fragmentation of size-asymmetric

systems is characterized by a three-peaked residue-mass distribution, two of the groups corresponding to the quasi-initial masses, and the third group to smaller satellite drops. Bradley & Stow (1979) qualitatively describe a dependence in the position of the lower quasi-initial mass group as a function of B, which is consistent with our quantitative measurements (figure 7). Concerning multiplicity, the direct dependencies of N_p with B and We shown in figure 6, are also similar to what has been reported by Brazier-Smith *et al.* (1972, see their figure 5), and Bradley & Stow (1979, see their figure 7) for water drops.

7. Models

The stability of systems formed when two drops collide has been the subject of extensive theoretical investigation. The general interest and sophistication of the models vary enormously depending on the field of application. In meteorology, for example, the concern is to understand the limiting conditions for permanent coalescence, i.e. the C-F boundary using simple mechanical arguments. Atomization and spray experts, more concerned with fragmentation, rely on fluid-dynamic models to understand their data. At the microscopic scale, molecular and nuclear physicists deal with collective aspects of clusters and nuclei as if they were drops, having developed sophisticated quantal and semi-quantal models which include important fluid-dynamic components. As we shall see, in one of those models the quantal and Coulomb effects can be cleanly 'switched off' allowing us to compare their predictions with experimental data from the macroscopic domain through the appropriate scaling. This section contains a brief review of those theories and their predictions.

7.1. *The upper C-F branch*

Since, as we shall see, most models predict that the upper C-F branch should follow (or nearly follow) the $1/We^{1/2}$ dependence observed experimentally (figures 14 and 15), the accuracy of the predictions in this respect can be better judged by the ability of each theory to reproduce the mean $\overline{We_u} = 7.19 \pm 3.24$ which is determined from the experimental data at $B = 1$ (see figure 16a). Another important aspect to be considered is the $\varDelta$-dependence predicted by the models which is compared with the corresponding data in figure 16(b).

7.1.1. *Neck vs. bulk-motion models*

The upper C-F branch for size-symmetrical systems was first interpreted by Adam *et al.* (1968) as due to a rotational instability. They observed that, before disruption, large-B-value systems assume a rotating dumb-bell shape, i.e. two large masses joined by an intermediate neck, rotating about the centre of mass. Based on this, they made an estimate for the onset of disruption at $B = 1$ by assuming that all the kinetic energy transforms into rotational energy. Under those conditions the stability of the dumb-bell was made to depend on whether the neck had sufficient strength to stand the centrifugal pull of the two (equal) external masses. Using an empirical critical neck shape, their prediction (Adam *et al.* 1968) corresponds to $We_u(\varDelta = 1) = 2.1$, a factor of ≈ 4 below the mean experimental value (figure 16).

Park (1970) modified the model to predict $B \leqslant 1$, and $\varDelta \geqslant 1$, values, by introducing an idealized B-dependent neck dimension and assuming conservation of angular momentum, instead of energy. The B vs. We dependence predicted by this model can

be calculated using the expressions

$$B_u = \left(\frac{12c}{\pi We}\right)^{1/2} \left[\frac{(1+\Delta^3)(1+\Delta^5)}{5\Delta^3(1+\Delta)} + \frac{(1+\Delta)}{2}\right] \tag{3}$$

where $c(B)$ is the neck variable

$$c = \left[4\Delta^2 - \left(B(1+\Delta) + \frac{(1-\Delta)}{B}\right)^2\right]^{1/4}.$$

These equations underestimate the data by predicting $We_u = 0$ for size-symmetric systems (figure 16a), while, like most other models, yielding a Δ-dependence for We_u (dotted curve in figure 16b) which increases more rapidly than observed.

More recently Ashgriz & Poo (1990), arguing that separation occurs much earlier than the development of any significant rotation, rejected the rotational limitation concept, proposing instead a model in which a fraction of the linear kinetic energy, termed 'stretching energy', is required to balance the surface attraction of a critical neck. Thus, as proposed by Adam *et al.* (1962), large-B disruption is said to occur whenever the sum of the linear kinetic energies of the non-overlapping masses and of the overlapping masses, weighted by B^2, exceeds the surface energy of the neck, approximated by a cylinder having the length $l = D(1 - B)$ and a mass equal to that contained in the projected overlapping volumes. This model results in high-order polynomials relating B to We which for $\Delta = 1$ can be reduced to

$$We(\Delta = 1) = 8[3(1-B)^3(1-2B)]^{1/2}. \tag{4}$$

Since, $B = 1$ implies no volume overlap (hence, no neck), this formulation predicts $We_u = 0$ for all Δ-values (see equation 32 of Ashgriz & Poo 1990).

7.1.2. *Energy balance model*

Brazier-Smith *et al.* (1972) proposed two models to interpret the upper C-F branch. One of them avoids complicated shape parametrizations by proposing that the system would be unstable when the rotational energy exceeds the surface energy necessary to form two (spherical) droplets out of the (spherical) coalesced system. This leads to the expression

$$B_u = \left[\frac{4.8f(\Delta)}{We}\right]^{1/2} \tag{5}$$

where

$$f(\Delta) = \frac{\left[1 + \Delta^2 - (1+\Delta^3)^{2/3}\right](1+\Delta^3)^{11/3}}{\Delta^6(1+\Delta)^2}$$

is a function which varies from 1.3 for $\Delta = 1$ to 2.2 for $\Delta = 1.65$. This model (Brazier-Smith *et al.* 1972) has been used extensively (Pruppacher & Klett 1978) as it provides a reasonable fit to most of the available upper C-F branch data, predicting a $We_u = 6.29$ for size-symmetric ($\Delta = 1$) systems, in good agreement with the experimental observations (see figure 16a). The corresponding prediction for the Δ-dependence of We_u, being more rapid than observed (solid curve in figure 16b), is the one that provides the best fit for this kind of data, failing only at the highest Δ-values.

7.1.3. *Shape evolution models*

The second model in Brazier-Smith *et al.* (1972) work is based on the similarity between the equilibrium configurations of a rotating liquid drop near the limiting angular momentum L_c for size-symmetric breakup, and the last stages of a large-B collision. This approach represents a conceptual improvement over the above-mentioned models because it takes into account not only the change in surface energy but also the change in moment of inertia between the equivalent sphere and the limiting dumb-bell configurations. The Brazier-Smith *et al.* (1972) estimate corresponds to

$$B_u = \left[\frac{\zeta(\Delta^3 + 1)^{13/6}}{\Delta^3(1 + \Delta)We^{1/2}} \right] \qquad (6)$$

with $\zeta = 4.26$. Unfortunately, this prediction grossly overestimates the experimental values, yielding $We_u(\Delta = 1) = 91.7$ with a Δ-dependence (not shown) more rapid than observed. These authors also noted that their predicted L_c values are a factor of 3.5 larger than the experimental values.

This connection between colliding drops and the equilibrium configurations of a rotating mass was studied in more detail by Cohen, Plasil & Swiatecki (1974, see also Swiatecki 1974) who calculated the total (surface+electric+rotational) potential energy surfaces to determine the saddle point for the symmetric 'fissioning' of an electrically charged rotating drop. When applied to uncharged masses, the Cohen *et al.* (1974) theory yields a $\zeta = 2.78$ to be used in equation (6), corresponding to $We_u(\Delta = 1) = 4.43$. This value, being 35% below the experimental one (figure 16) is clearly in better agreement than what Brazier-Smith *et al.* (1972) estimated within the same theoretical framework. Still, the L_c values predicted by the Cohen *et al.* (1974) theory are, typically, a factor of 2 larger than the experimental observations (figure 16). On this problem, our group (Menchaca-Rocha *et al.* 1993, see also Cuevas *et al.* 1993) used a three-dimensional surface potential model developed more recently by Blocki & Swiatecki (1982) to search for the L-values at which the energy pocket disappears. Although this new approach still gave larger than expected L_c, we have shown (Menchaca-Rocha *et al.* 1993, see also Cuevas *et al.* 1993) that the overestimation can be reduced by introducing, in a simplified way, dynamical effects. An interesting way of doing so was proposed by Schmidt & Lutz (1992). Based on the Cohen *et al.* (1974) saddle point calculations, they argue that the complex deformations observed in colliding systems result in shallow potential multidimensional energy surfaces. Thus disruption is said to set in when the centrifugal+surface energy barrier located at the saddle is overcome by the total collective energy of the equivalent spherical complex. Schmidt & Lutz (1992) also extended this type of calculation to predict the upper C-F branch. In our notation, their (Schmidt & Lutz 1992) result can be written as

$$B_u = \left[\frac{24}{5} \frac{(\Delta^3 + 1)^{13/3}}{\Delta^6(\Delta + 1)} \frac{Y_c}{We} \right] \qquad (7)$$

where $Y_c = 0.38$, which yields $We_u(\Delta = 1) = 9.19$, which lies within the experimental value (figure 16*a*); however, its predicted Δ-dependence (as all others) increases faster that observed (dashed curve in figure 16*b*).

In general, however, the calculations based on the limit of stability of a rotating drop assume that the colliding droplets form a rotating system which smoothly undergoes symmetric breakup as a rotating (equivalent) spherical drop would, with no loss of energy to either internal or vibrational degrees of freedom. This approach has serious limitations. First, symmetric two-droplet outcomes are only observed

for $\Delta = 1$ collisions in a limited Weber number range (see figure 8). Second, the initial stages of the collision induce vibrational modes which should also play a role in determining the outcome. Finally, it is not clear why the loss of energy to non-rotational modes should be negligible. An alternative approach, which deals with some of these problems was proposed by Ryley & Bennett-Cowell (1967) who focused on those energy-damping vibrational modes by proposing that the surface of the temporarily coalesced system oscillates adopting extreme shapes, represented by three model surfaces (their figure 4). When enough energy is available for fragmentation to occur, this is assumed to proceed via the formation of a stretched spherically ended cylinder (one of the three model shapes) subject to Rayleigh instabilities. However, their theoretical prediction (Ryley & Bennett-Cowell 1967) for the rate of energy dissipation is based on parameters (the surface area of each extreme shape and the angular velocity) to be determined experimentally, thus resulting in a model with little predicting power.

One last approach we would like to mention is that of Arkhipov *et al.* (1983) who, based on the evolution of the surface shapes, used a variational principle to determine the point at which the effective (surface+rotational) potential between the two droplets loses its attractive minimum. The corresponding prediction is

$$B_u = \frac{1}{\Delta^3} \left[\frac{6(1 + \Delta^3)}{We} \right]^{1/2}. \tag{8}$$

By setting $B = \Delta = 1$ and solving for We in (8) one obtains a $We_u(\Delta = 1) = 12$ prediction, 50% higher than the mean experimental value (figure 16*a*); however, against the experimental evidence (dot-dashed curve in figure 16*b*), this theory predicts that We_u should be a rapidly decreasing function of Δ.

7.1.4. *The effect of 'rolling'*

We now estimate the effect that the 'rolling' motion could have on the upper C-F branch in the present mercury-drop experiments. For simplicity, the calculations will be based on the energy-balance ideas of Brazier-Smith *et al.* (1972) which state that the upper C-F branch reflects the equilibrium between the rotational and the surface energies (see §7.1.2). As mentioned previously (§4), the rolling motion introduces a rotational energy, not always present in collisions between free-moving drops. Since the liquid masses rotate in opposite directions, upon contact the connecting neck is subjected to a twisting motion which tends to lower its cohesive strength. We assume that a fraction F of this rolling energy enhances the breaking up of the system. Thus the equilibrium condition now becomes

$$E_{rot} + F E_{roll} = \sigma(S_f - S_i) \tag{9}$$

where the left-hand side of the equation represents the rotational and the fraction of the rolling energies, and the right-hand side, the surface energy change. Using spherical shapes to estimate the moments of inertia, and assuming equal linear momentum for both drops (a good approximation in our experimental situation), the resulting equation for the upper C-F branch is

$$B(We) = \left[\frac{4.8 f(\Delta)}{We} - F f'(\Delta) \right]^{1/2} \tag{10}$$

with $f(\Delta)$ as defined in (5) and

$$f'(\Delta) = 0.16 \, \frac{(1 + \Delta^3)^{5/3}}{\Delta^3(1 + \Delta^2)}.$$

Since, as expected, in the $E_{roll} = 0$ limit, (10) becomes (4), we have used its parametric form:

$$B(We) = \left[\frac{We_u}{We f(\Delta)} - F f'(\Delta) \right]^{1/2} \tag{11}$$

(leaving F as free parameter), as well as (5) to fit the data in $16(a, b)$, and the results are shown in figure $13(a, b)$ as solid and dashed curves, respectively. The values obtained using the non-rolling approximation (equation (5)) are $We_u = 6.65$, for $\Delta = 1$, and 8.58 for $\Delta = 1.65$, while the corresponding fits, assuming rolling (equation (11)), yielded $We_u = 8.32$ (with $F = 0.43$) and 11.02 (with $F = 0.75$), i.e. $\approx 20\%$ higher We_u than in the non-rolling case. Although, given the large fluctuations shown in figure 16, both sets of values lie within the experimental range reported for free-moving drops, we took the improved overall fit to mercury-drop data as a justification for using the rolling values shown in figure $16(a, b)$.

7.2. *Other observables*

By assuming that the energy dissipated during the collision is proportional to the overlapping masses, the Ashgriz & Poo (1990) model can be used to provide a prediction for the B-dependence of the energy loss, as illustrated by the solid curves in figure $10(c, f)$.

It is also interesting to note that the B-dependence of the mass distributions shown in figure $8(d$–$f)$ is consistent with a qualitative description given by Ashgriz & Poo (1990) concerning two competing effects, termed 'drainage' and 'stretching', in mass transfer among asymmetric systems. When the contact time is long enough, as in the most central collisions, drainage is said to appear because of the difference in internal pressure. This would produce a mass flow from the small to the large drop, separating the mass groups. On the other hand, for short contact times, characteristic of the more peripheral collisions, stretching is said to occur because, with no time for pressure equilibration, the large drop appears softer to the small drop, so that the small drop can 'scoop' mass from the large drop. In figure $8(d$–$f)$ we see that, as B is decreased from 1 to 0.4, the quasi-initial masses approach, as would be expected for stretching flow, and then separate rapidly at lower B-values as has been argued (Ashgriz & Poo 1990) to happen in drainage.

7.3. *Fragmentation*

The few existing theoretical approaches to fusion–fission type fragmentation can be classified as surface-dynamic and volume-dynamic.

7.3.1. *Surface-dynamic model*

Time-dependent fragmentation calculations in which the state of the system is followed as it travels (dissipating energy) through a potential energy landscape have also been attempted. One example of this surface-dynamic approach is the model of Cârjan *et al.* (1986), originally developed to simulate nuclear reactions, which we modified for its application to macroscopic drops (Menchaca-Rocha *et al.* 1995). In it, the shape of the system (necessary to calculate the surface energy, and the inertia and dissipation tensors) is represented by an axially- and reflection-symmetric

Legendre-polynomial parametrization:

$$\rho_s^2(z) = R_o^2 \sum_{k=0}^{K} q_k P_{2k}(z/z_0) \tag{12}$$

where z is the coordinate along the symmetry axis, ρ_s is the distance perpendicular to the symmetry axis, z_o is one-half the distance between the two ends of the shape, R_o is the radius of the spherical drop having the mass of the coalesced system, P_{2k} is a Legendre polynomial of degree $2k$, while the q_k (for $k > 0$) are the K-independent symmetric shape coordinates. Assuming incompressibility, the quantity q_o is determined by volume conservation. The results discussed here are restricted to $K = 5$.

In these calculations, the potential energy of the system is composed of an attractive surface, and a repulsive centrifugal term. The collective kinetic energy is given by

$$T = 0.5 M_{ij}(q)\dot{q}_i\dot{q}_j = 0.5[M(q)^{-1}]_{ij} p_i p_j \tag{13}$$

where $M_{ij}(q)$ is the shape-dependent inertia tensor. The collective momenta p are related to $\dot{q}$ and M_{ij} through

$$p_i = M_{ij}(q)\dot{q}_j. \tag{14}$$

The internal degrees of freedom are represented by a dissipative force having a mean component in the ith direction:

$$F_i = -\eta_{ij}(q)\dot{q}_j \tag{15}$$

where $\eta_{ij}(q)$ is the shape-dependent dissipation tensor $\eta(q)$.

With the above ingredients, the generalized Hamilton equations of motion were solved to determine the time evolution of the system. A typical CPU time for one macroscopic drop collision simulation is 10 s in a CRAY XMP computer.

In figure 17 we illustrate what is predicted by the dynamical model for a mercury-drop collision having the same initial conditions as the event shown in figure 3(f). A restriction imposed by the shape parametrization (12) implies that the time evolution predicted by the model begins and ends when the initial and final necks reach a small but finite value, i.e. the simulation starts when the drops are already in contact and stops when the outermost necks reach the limiting diameter. Besides that, and the fact that the real shapes are more complex, the overall features of the observed time sequence seem to be well reproduced by the model: there are three bodies in the final state, and the system separates at a similar angle. There are, however, two important differences: the predicted interaction time is approximately one-third of what is observed, and the relative size of the drops is less well reproduced, i.e. the model predicts neck particles which are bigger than the observed ones. The latter is better seen in figure 18 showing the predicted B-dependence of the mass of the residues, normalized to the total mass m_i/m_t, which should be compared with figure 8(a–c). The larger mass of the middle drops and the faster time evolution predicted could be expected to result from the assumption of rigid rotation implicit in the model, placing all the available angular momentum in whole-body rotation. Thus the system is predicted to rotate faster and stretch longer. The model provides predictions for other $\Delta = 1$ observables with different degrees of success. The mean multiplicity distributions, shown as solid and dashed lines in figure 6(a) (see caption), are examples of this.
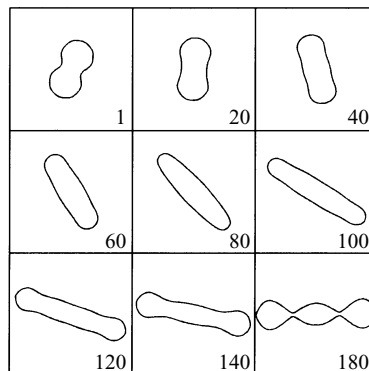
FIGURE 17. Predicted time evolution for a $\varDelta = 1$ mercury-drop collision with $B = 0.7$ and $We = 35$, conditions which are similar to those of figure 3(f). The initial drops move against each other in the horizontal direction, while the time runs as indicated, in units of 0.325 ms, approximately three times faster than the experimental case (figure 3f).
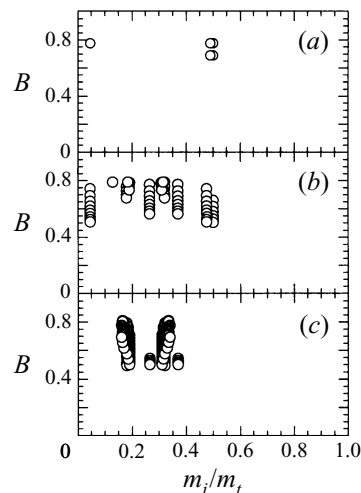

FIGURE 18. Predicted residue-mass distributions for $\varDelta = 1$ systems, as a function of B and We, following the same conventions as in figure 8.

7.3.2. *Volume-dynamic models*

The volume-dynamic approach involves the complex task of solving equations of three-dimensional unsteady fluid flow with free surfaces. Solutions of the so called Boltzmann–Uhleing–Uhlenbeck and the Landau–Vlasov equations have been very successful in explaining observables in nuclear reactions (i.e. Aichelin *et al.* 1988) and molecular cluster (Guilleumas *et al.* 1993 and references therein) collisions. Unfortunately in these formulations the quantum-mechanical aspects are not easily separable from the purely fluid-dynamic ones.

Concerning macroscopic (non-quantal) systems the problem is generally tackled using the finite difference method of solving the Navier–Stokes equations in the bulk. The surface evolution is, then, dealt with in an *ad-hoc* way using interface tracking procedures. One such approach, developed by Lafaurie *et al.* (1994), has been used to simulate (peripheral and central) coalescence drop collisions, resulting in shape evolutions which are very similar to what we observe (compare their figures 17 and

18 with our figure 3*a, b*). Unfortunately, due in part to the large CPU costs involved (hours and even days per collisions), those hydrodynamic codes have not been used to provide detailed predictions for fragmentation observables (N_p, m_r, etc.). We would like to mention that faster, two-dimensional, simulations by Poo & Ashgriz (1992), and Lafaurie *et al.* (1994), have been shown to reproduce well the surface evolutions observed in three-dimensional liquid-drop experiments.

8. Conclusions

The fragmentation occurring in the collisions of mercury-drop pairs which move on a horizontal glass surface has been studied experimentally. A new technique is presented in which the drop formation and the acceleration stages are decoupled, allowing precise measurements of the most relevant initial parameters (masses, impact parameter and relative velocity). By restricting the motion of the collision residues to the horizontal plane the new method also permits a precise determination of important final parameters, such as the mass, speed and direction of each residue. An event-by-event-type analysis was introduced to extract the statistics and correlations of the various parameters. By comparing the results from the present mercury-drop experiments to what is known from more standard techniques, involving free-moving drops, we find that the influence of the glass surface (the price paid to obtain this unprecedented amount of information from each collision) does not significantly change the phenomenology, particularly of the non-central collisions. The use of larger (a few mm diameter) and more dense drops implied lower velocities for a given We, thus reducing the aerodynamic effects to such a degree that no appreciable bouncing collisions are observed. The analysis from 500 size-symmetric and 500 size-asymmetric collisions using this mercury-drop technique, and of other data, shows that, below a critical Weber number, We_u (≈ 7 for size-symmetric systems and $\leqslant 15$ for $\varDelta \leqslant 3$), all collisions result in coalescence, while beyond that point fragmentation appears, first in the off-centre collision region and, eventually, expanding to all impact parameters. One characteristic of drops moving on a solid surface is that, in head-on collisions, a liquid column (instead of a disk) is formed in a direction perpendicular to the collision trajectory which breaks up beyond a critical value, We_l (≈ 90 for $\varDelta = 1$ systems). As in collisions involving free-moving drops in the same $0.5 \leqslant We \leqslant 125$ regime, the mass distribution of fragments is characterized by two large residues, having masses similar to those of the initial drops, and a number of smaller fragments produced in the intermediate neck region. Yet, our measurements as a function of the impact parameter now show that the mass of some of those neck fragments increases as the impact parameter decreases and that the largest number of drops occurs in the $0.5 \leqslant B \leqslant 0.7$ impact parameter range. The data from collisions between unequal drops also show that no appreciable mass transfer occurs, except at the lower impact parameters where the large drop draws mass from the smaller one. Concerning the speed of the residues, it was found that it has an inverse correlation with the angle at which the fragments are emitted and a direct correlation with the impact parameter. The dissipated energy was shown to be closely correlated with the impact parameter, following a dependence which resembles that of the overlapping volumes. The present experimental data, along with those reported in the literature for other liquids of similar kinematic viscosity, were used to test the validity of We scaling for drop-collision phenomena. The theoretical situation concerning existing hydrostatic drop collision models, mostly developed to understand the limits of coalescence, was reviewed, and the corresponding predictions were compared with the experimental

data. Finally, a surface-dynamic nuclear fragmentation model, adapted by us for its use in macroscopic drop collisions, was presented, and it was shown to reproduce some aspects of the observed phenomena.

REFERENCES

ADAM, J. R., LINDBLAD, N. R. & HENDRICKS, C. D. 1968 The collision, coalescence and disruption of water droplets. *J. Appl. Phys.* **39**, 5173.

AICHELIN, J., PEILERT, G., BOHNET, A., ROSENHAUER, A., STÖCKER, H. & GREINER, W. 1988 Multi-fragmentation and the nuclear equation of state. *Nucl. Phys.* A **488**, 437c.

ARKHIPOV, V. A., VASENIN, I. M. & TROFIMOV, V. F. 1983 Stability of colliding drops of ideal liquid. *Zh. Prikl. Mekh. Tekh. Fiz.* **3**, 95.

ASHGRIZ, N. & GIVI, P. 1987 Collision dynamics of fuel droplets. *Intl J. Heat Fluid Flow* **8**, 205.

ASHGRIZ, N. & POO, J. Y. 1990 Coalescence and separation in binary collisions of liquid drops. *J. Fluid Mech.* **221**, 183.

BLOCKI, J. & SWIATECKI, W. J. 1982 Nuclear deformation energies according to a liquid drop model with a sharp surface. *Lawrence Berkeley Laboratory Preprint* 12811-UC-34d.

BRADLEY, S. G. & STOW, C. D. 1979 On the production of satellite droplets during collisions between water drops falling in still air. *J. Atmos. Sci.* **36**, 495.

BRAZIER-SMITH, P. R., JENNINGS, S. E. & LATHAM, J. 1972 The interaction of falling water drops: coalescence. *Proc. R. Soc. Lond.* A **326**, 393.

BRENN, G. & FROHN, A. 1989 Collision and merging of two equal droplets of propanol. *Exps. Fluids* **7**, 441.

CÂRJAN, N., SIERK, A. J. & NIX, J. R. 1986 Effect of dissipation on ternary fission in very heavy nuclear systems. *Nucl. Phys.* A **452**, 381.

COHEN, S., PLASIL, F. & SWIATECKI, W. J. 1974 Equilibrium configurations of rotating charged or gravitating liquid masses with surface tension II. *Ann. Phys.* **82**, 557.

CUEVAS, A., CHAPA, M., SILVA, M. & MENCHACA-ROCHA, A. 1993 Fission of drops induced by angular momentum. *Rev. Mex. Fis.* **39**, 428.

GUILLEUMAS, M., GRACIAS, F., BARRANCO, M., PI, M. & SURAUD, E. 1993 Static aspects of fission and fusion of ^{3}He drops. *Z. Phys.* D **25**, 227.

JIANG, Y. J., UMEMURA, A. & LAW, C. K. 1992 An experimental investigation on the collision behaviour of hydrocarbon droplets. *J. Fluid Mech.* **234**, 171.

LAFAURIE, B., NARDONE, C., SCARDOVELLI, R., ZALESKI, S. & ZANETTI, G. 1994 Modelling merging and fragmentation in multiphase flows with SURFER. *J. Comput. Phys.* **113**, 134.

LIST, R., MACNEIL, C. F. & MCTAGGART-COWAN, J. D. 1970 Laboratory investigation of temporary collisions of raindrops. *J. Geophys. Res.* **75**, 7573.

MCTAGGART-COWAN, J. D. & LIST, R. 1975 Collision and breakup of water drops at terminal velocity. *J. Atmos. Sci.* **32**, 1401.

MENCHACA-ROCHA, A. 1992 The mobility of mercury drops on rough glass surfaces. *J. Colloid Interface Sc.* **114**, 472.

MENCHACA-ROCHA, A., BRANDAN, M. E., GUTIÉRREZ, M. & LABBÉ, R. 1986 Liquid drop collider to simulate nuclear reactions. *The Physics Teacher* **24**, 102.

MENCHACA-ROCHA, A., CUEVAS, A., CHAPA, M. & SILVA, M. 1993 Rotating-liquid-drop model limit tested on macroscopic drops. *Phys. Rev.* E **47**, 1433.

MENCHACA-ROCHA, A., HUIDOBRO, F., MICHAELIAN, K., PÉREZ, A., RODRIGUEZ, V. & CÂRJAN, N. 1995 From nuclei to liquid drops. In *Heavy-ion Dynamics and Hot Nuclei, Proc. Annual Meeting of the American Chemical Soc., Nuclear Chem. Award Symposium, Anaheim, Ca* (ed. G. Nebbia & M. N. Namboodiri). World Scientific.

OCHS, H. T., CZYS, R. R. & BEARD, K. V. 1986 Laboratory measurement of coalescence efficiencies for small precipitation drops. *J. Atmos. Sci.* **43**, 225.

PARK, R. W. 1970 Behaviour of water drops colliding in humid nitrogen. PhD Thesis, Dept. of Chemical Engineering, University of Wisconsin.

PARK, R. W. & CROSBY, E. J. 1965 A device for producing controlled collisions between pairs of drops. *Chem. Engng Sci.* **20**, 39.

PLATEAU, J. 1873 *Statistique Expérimentale et Théorique des Liquides soumis aux Seules Forces Moléculaires*, Vol. 2, Gauthier-Villars.

PODVYSOTSKY, A. M. & SHRAIBER, A. A. 1984 Coalescence and breakup of drops in two-phase flows. *Intl J. Multiphase Flow* **10**, 1195.

POO, J. Y. & ASHGRIZ, N. 1991 Variation of drag coefficients in an interacting drop stream. *Exps. Fluids* **11**, 1.

POO, J. Y. & ASHGRIZ, N. 1992 Numerical simulation of collision of two-dimensional drops. In *Proc. 5th Annual Conf. on Liquid Atomization and Spray Systems, San Ramon, Ca.*, p. 110.

PRUPPACHER, H. P. & KLETT, J. D. 1978 *Microphysics of Clouds and Precipitation.* D. Reidel.

QIAN, J. & LAW, C. K. 1997 Regimes of coalescence and separation in droplet collision. *J. Fluid Mech.* **331**, 59.

RAYLEIGH, LORD 1882 Further observation upon liquid jets, in continuation of those recorded in the society's proceedings for March and May, 1879. *Proc. R. Soc. Lond.* A **34**, 130.

RYLEY, D. J. & BENNETT-COWELL, B. N. 1967 The collision behaviour of steam-borne water drops *Intl J. Mech. Sci.* **9**, 817.

SALITA, M. 1991 Use of water and mercury droplets to simulate Al_2O_3 collision/coalescence in rocket motors. *J. Propulsion Power* **7**, 505.

SCHMIDT, R. & LUTZ, H. O. 1992 Fusion and stability of colliding atomic nuclei, atomic clusters and liquid droplets. *Phys. Rev.* A **45**, 7981.

STERNIN, P. E. & SHRAIBER, A. A. 1994 *Multi-phase Flow of a Gas with Particles.* Publ. Mashinos-troerie, Moscow.

SWIATECKI, W. J. 1974 The rotating, charged or gravitating liquid drop, and problems in nuclear physics and astronomy. In *Proc. Intl Colloq on Drops and Bubbles* (ed. D. J. Collins, M. S. Plesset & M. M. Saffren), p. 52. Publ. Jet Propulsion Laboratory, Pasadena CA.

VASENIN, I. M., ARKHIPOV, V. A., BUTOV, V. G., GLAZUNOV, A. A. & TROFIMOV, V. F. 1986 *Gas Dynamics of Two Phase Flow.* Tomsk University Press.

VASSALLO, P. & ASHGRIZ, N. 1991 Satellite formation in liquid jet breakup. *Proc. R. Soc. Lond.* A **433**, 269.

WANG, T. G. 1988 (Ed.) *Proc. Third Intl Coll. on Drops and Bubbles, Monterey, Ca.*, AIP Conf. Proc. 197.

YULE, A. J. & DUMOUCHEL, CH. 1994 (Eds.) *Proc. Sixth Intl Conf. on Liquid Atomization and Spray Systems, Rouen, France.* Begell House, Inc.